Tectonic and Anthropogenic Deformation at the Cerro Prieto Geothermal Step-Over Revealed by Sentinel-1A InSAR

Xiaohua Xu, David T. Sandwell, Ekaterina Tymofyeyeva, Alejandro González-Ortega, and Xiaopeng Tong

***Abstract*— The Cerro Prieto geothermal field (CPGF) lies at the step-over between the imperial and the Cerro Prieto faults in northern Baja California, Mexico. While tectonically this is the most active section of the southern San Andreas Fault system, the spatial and temporal deformation in the area is poorly resolved by the sparse global positioning system (GPS) network coverage. Moreover, interferograms from satellite observations spanning more than a few months are decorrelated due to the extensive agricultural activity in this region. Here we investigate the use of frequent, short temporal baseline interferograms offered by the new Sentinel-1A satellite to recover two components of deformation time series across these faults. Following previous studies, we developed a purely geometric approach for image alignment that achieves better than 1/200 pixel alignment needed for accurate phase recovery. We construct interferometric synthetic aperture radar time series using a coherence-based small baseline subset method with atmospheric corrections by means of common-point stacking. We did not apply enhanced spectral diversity because the burst discontinuities are generally small (<1.4 mm) and can be effectively captured during the atmospheric corrections. With these algorithms, the subsidence at CPGF is clearly resolved. The maximum subsidence rate of 160 mm/yr, due to extraction of geothermal fluids and heat, dominates the ~40 mm/yr deformation across the proximal ends of the imperial, the Cerro Prieto, and the indiviso faults.**

***Index Terms*— Atmospheric correction, geometric coregistration, land subsidence, synthetic aperture radar (SAR) interferometry (InSAR), tectonic deformation, terrain observation by progressive scan (TOPS), time series.**

I. Introduction

The Cerro Prieto geothermal field (CPGF) is the second largest geothermal field in the world with an average annual net fluid extraction over ten million tons. As a consequence, the surface subsides at an extraordinary rate despite the fact that the reservoir is deep and isolated from groundwater [40]. Surrounding the CPGF, the fault system is complex. The northeast end of the CPGF connects to the Imperial fault while the southwest end reaches the Cerro Prieto fault. The Indiviso fault, where the 2010 El-Mayor Cucapah earthquake rupture took place, is only 15 km to the west [12]. Previous estimates of the subsidence rate at CPGF are up to 120–140 mm per year [8], [14], [29], [30], [38], and the expected horizontal deformation across the Imperial fault and the Cerro Prieto fault is around 40 mm per year [2]. Tectonically, this is the most active zone of the southern San Andreas Fault system, but the spatial and temporal deformation for this area is poorly resolved. Part of the reason is the lack of global positioning system (GPS) data coverage, and the fact that observations from interferometric synthetic aperture radar (InSAR) are often biased due to the decorrelation introduced by extensive agricultural activity (InSAR tutorial can be found in [22] and [34]).

To overcome these challenges, we use synthetic aperture radar (SAR) data from the C-band Sentinel-1A satellite operated by the European space agency (ESA). Sentinel-1A was launched on April 3, 2014, and has been in routine operation for about two years. The satellite is capable of revisiting a prioritized area (such as CPGF) with every 12 days, primarily with a burst radar acquisition mode called terrain observation by progressive scan (TOPS). For other areas, the revisit time is usually 24 days. While the short revisit time is achieved by using TOPS mode, this new type of acquisition mode brings challenges to data processing. Following previous studies [11], [23], we developed a geometric alignment approach using postprocessed precise orbits of Sentinel-1A (~50 mm along-track and ~20–30 mm cross-track [7]). We performed a systematic analysis to test the capabilities of this data set, and used coherence-based small baseline subset (SBAS) [36] and atmospheric correction with common-point stacking [39] to calculate the deformation time series around CPGF. The potential burst discontinuities caused by miss-registration along azimuth were handled during the atmospheric correction step instead of directly applying enhanced spectral diversity (ESD) after geometric alignment, taking advantage of the errors being randomly distributed in time. With these algorithms, the maximum subsidence velocity at the CPGF is clearly resolved ~160 mm/yr and the tectonic deformation rate across this region is ~40 mm/yr.

Manuscript received November 7, 2016; revised March 15, 2017 and April 21, 2017; accepted May 4, 2017. Date of publication June 5, 2017; date of current version August 25, 2017. This work was supported in part by the NASA Earth Surface and Interior Program under Grant NNX16AK93G, in part by the National Science Foundation (NSF) Geoinfomatics Program under Grant EAR-1347204, and in part by the Southern California Earthquake Center (SCEC) through the NSF cooperative under Agreement EAR-1033462 and through the U.S. Geological Survey Cooperative under Agreement G12AC20038. *(Corresponding author: Xiaohua Xu.)*

X. Xu, D. T. Sandwell, and E. Tymofyeyeva are with the Institute of Geophysics and Planetary Physics, Scripps Institution of Oceanography, University of California San Diego, La Jolla, CA 92093 USA (e-mail: xix016@ucsd.edu).

A. González-Ortega is with the Centro de Investigacion Cientifica y de Educacion, Ensenada 22806, Mexico.

X. Tong is with the Department of Earth and Space Science, University of Washington, Seattle, WA 98105, USA.

This paper has supplementary downloadable material available at http://ieeexplore.ieee.org, provided by the author.

Color versions of one or more of the figures in this paper are available online at http://ieeexplore.ieee.org.

Digital Object Identifier 10.1109/TGRS.2017.2704593

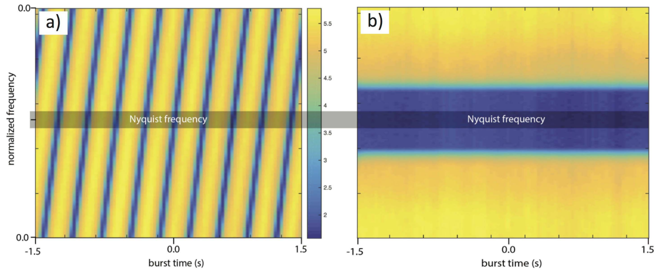

Fig. 1. Spectrogram of one burst of TOPS-mode data plotted on a log color scale. (a) Original spectrogram of a single burst of TOPS data wraps around the Nyquist frequency nine times. (b) Spectrogram after deramping has low power close to the Nyquist, which enables accurate resampling.

II. Sentinel-1 TOPS Processing

The Sentinel-1 mission was designed to acquire frequent observations (12 or 24 days) with Interferometric Wide Swath (∼250 km) product using TOPS mode [37]. Unlike conventional scanning synthetic aperture radar, which illuminates the ground with a series of separated bursts, the TOPS mode SAR system rotates its antenna during the observation of each burst. While this type of observation reduces the along-track amplitude scalloping (signal-to-noise ratio change), it also introduces azimuthally varying Doppler centroid [23]. The Doppler centroid variation (∼4.5 kHz) wraps the satellite pulse repetition frequency (PRF∼486 Hz) nine times (Fig. 1). Due to this feature, the azimuth miss-registration error has to be better than 1/200th of a pixel (i.e., 66 mm) to keep the phase difference at burst boundaries to less than 1.4 mm. Note that standard image cross-correlation methods only achieve ∼1/10 pixel accuracy, which would result in an unacceptably large phase mismatch of 28 mm at burst boundaries [4]. Moreover, the extra Doppler centroid goes beyond the Nyquist frequency, so accurate interpolation of the slave image into the master coordinates is not possible without deramping the slave, as discussed in [20].

We have implemented a robust coregistration method based on the geometric approach and optional ESD described in previous studies [28], [44]. The code is available as a new preprocessing module in GMTSAR http://gmt.soest.hawaii.edu/projects/gmt5sar. The preprocessing starts with a pixelwise estimate of range and azimuth offsets using precise orbits and a downsampled (∼360 m) digital elevation model (DEM), which covers the region of the single look complex (SLC) satellite images (step 1 in Fig. 2). The precise orbit is used to back-project each pixel in the DEM (lon, lat, ellipsoidal height) into the range and azimuth coordinates of the master and slave images (r, a). The algorithm first uses a golden section search method [24] to quickly find the closest point at the PRF sampling (∼14.5 m along-track) between the orbital trajectory and the topography pixel. Then a polynomial refinement algorithm is used to improve the numerical accuracy to better than 10 mm in the azimuth coordinate. The range coordinate is the range between the antenna and the topography pixel evaluated at the corresponding azimuth coordinate. Note that the range-rate or Doppler is zero at this closest point. (A correction for alignment to a nonzero Doppler is discussed in the GMTSAR documentation [27]). The differences between the range $\Delta r(r, a)$ and azimuth $\Delta a(r, a)$ of the slave image with respect to the master image are used to construct a dense look-up map of range and azimuth shifts, using a surfacing technique described in [Smith and Wessel, 1989]. After these maps are generated, the coregistration is done pixelwise, which accounts for topography variation across the full image.

The second step in the processing is to resample the slave image into the coordinates of the master image (step 2 in Fig. 2). Prior to resampling with a 2-D sync function, the slave image is deramped and demodulated following the algorithm in [Miranda 2015]. Best results are achieved if the deramping and reramping are only performed on slave image, leaving the master image unchanged. Using this approach, any possible inaccuracies in the deramping function will introduce no error because each slave is reramped using the conjugate of the original deramp function plus an appropriate phase shift related to the azimuth shift. Deramping, interpolation, and reramping are performed burst by burst, after which all bursts within one subswath are stitched to generate one aligned SLC image.

The third (optional) step in the processing is to use the ESD approach to refine the overall azimuth shift Δa_{ESD}. This follows the method described in previous studies [5], [44]. The burst overlap areas are extracted from the aligned master and slave SLC's and a double-difference interferogram is formed. Azimuth filtering is used to estimate phase, after which the coherence and the median of the phase for all the burst overlaps are used to estimate the phase shift using equation S1 in the Supplementary Material. ESD estimation is available in GMTSAR, so the user can decide when it is needed. The advantages and disadvantages of using ESD are discussed below.

The final step is to use any pair of aligned slave images to form an interferogram. We deburst the SLC's by removing half of the lines along the lower overlap zone of the first burst and half of the lines along the upper overlap zone of the second burst to form continuous SLC files. The full-resolution DEM, mapped into the range and azimuth coordinates of the reference image, is used to form a full-resolution interferogram with the topographic contribution removed. At this point, the user can decide on the type of spatial filter used to estimate phase, coherence, and amplitude. In the examples below, we use a Gaussian filter with a 0.5 gain at a wavelength of 300 m in azimuth and ground range. The interferometric products are sampled at 1/4 of the filter wavelength or smaller (<75 m). Each subswath is processed independently and then stitched in radar coordinates. Phase unwrapping is performed in radar coordinates. The results presented below were geocoded at four arc-seconds resolution.

The only significant differences between this approach and the approach described in [44] are that we do not perform common-band filtering in range or azimuth, and we use geometric alignment instead of patch cross correlation in range. We have tested both range alignment approaches and find that they work equally well. One potential advantage of the geometric range alignment approach is that it provides a pixelwise topographically dependent range shift, but that is

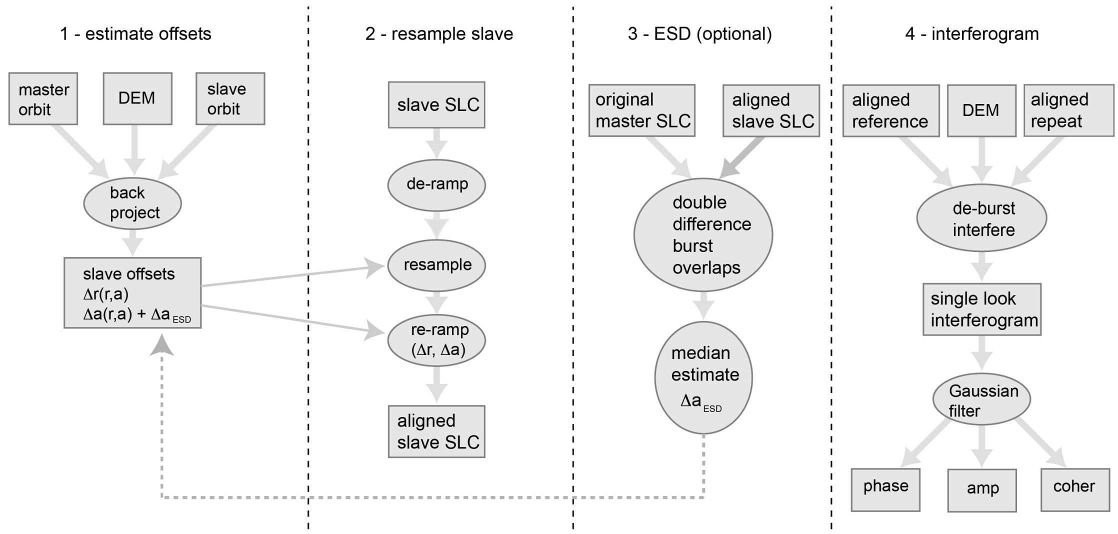

Fig. 2. Processing chain for TOPS data using precise orbits and point-by-point geometric coregistration. The ESD algorithm is implemented in GMTSAR but not used in this paper.

only needed when the baseline approaches a large fraction of the critical baseline, which does not happen for Sentinel-1 satellites.

There are two important advantages to this pure geometric coregistration approach. The first is that it does not require any phase coherence between the master and slave images. This will become increasingly important as the time separation between the master and the newly acquired slaves increases beyond several years. The second advantage is that after each slave is aligned to the same single master image, interferograms can be constructed from any two images in the set without needing further coregistration. This is confirmed below and in the Supplementary Material (Figs. S3 and S6), where we show that the sum of the phase of interferograms in closed circuits is zero to within the phase noise of the radar. This enables the construction of long deformation time series from short-timespan interferograms. Moreover, this greatly improves the efficiency in data processing since all images need only be aligned once to a single master.

After point-by-point geometric coregistration, the typical discontinuity between bursts is 1/400th of pixel (Table S1 in the Supplementary Material). Larger burst discontinuities are occasionally visible but they are not a constant azimuth shift at all the burst boundaries as expected [5], [32]. These burst discontinuities are potentially due to spatial variations in the ionosphere or clock error on certain bursts [6], [9].

To illustrate the accuracy of the geometric alignment as well as the subswath-to-subswath fidelity of the Sentinel-1 radar, we show a typical TOPS-mode interferogram (i.e., three subswaths) combined in geo-coordinates, which covers a very large area (∼250 km cross-track, ∼750 km along-track), from the Sierra Nevada Mountains across the Central Valley to the beach at Santa Barbara (Fig. 3). The acquisitions come from relative orbit number (track) 144 on date July 6, 2015 and July 30, 2015. The interferogram was processed with pure geometric alignment/coregistration and no extra adjustment from ESD [23]. Within this large area, the phase is visually continuous across burst and subswath boundaries.

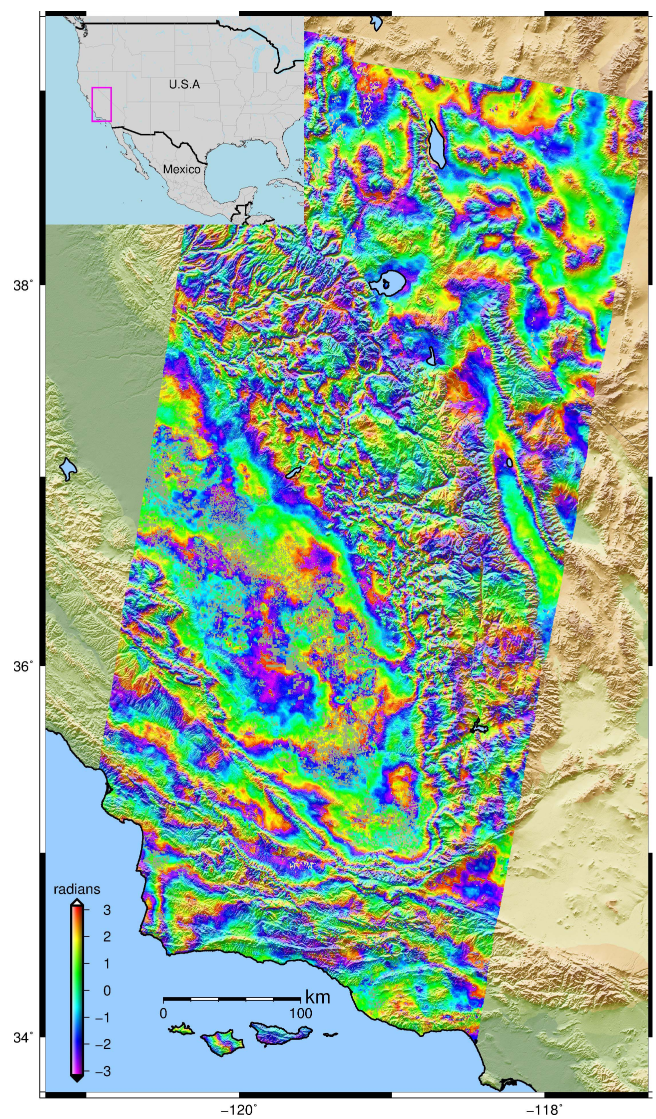

Fig. 3. Interferogram combining three subswaths (109 bursts) from track 144 of Sentinel-1A data, processed with GMTSAR with geometric alignment/coregistration. No ESD or swath-boundary adjustments were applied.

When observed at such a large scale, it is clear that the interferogram contains a significant amount of atmospheric noise, some of which is strongly correlated with topography. Also, even though the time-span of the interferogram is only 24 days, there is already some decorrelation around the farms in the Central Valley.

III. Estimation of InSAR Time Series at the CPGF

To investigate the evolution of the subsidence at CPGF, and the spatial and temporal deformation across the nearby faults, we processed InSAR data from the Sentinel-1A satellite spanning the period from October 2014 to July 2016. The satellite collected 42 acquisitions on descending track 173 and 36 acquisitions on ascending track 166. We constructed 201 interferograms from the descending scenes and 183 from the ascending scenes, with a 90-day temporal threshold and a 200-m perpendicular baseline threshold (Figs. 4 and S2 in the Supplementary Material). We did not use the ESD method [23], because the phase discontinuities at burst boundaries were much smaller than the atmospheric phase contributions (Table A1 and Figs. S3 and S4 in the Supplementary Material), and could be effectively removed along with the atmospheric signals as described below. To confirm that ESD is not needed, we also performed the analysis using ESD and compared the results (Fig. S8 in the Supplementary Material). The differences in average velocity are generally less than 1 mm/yr.

C-band data from SAR observations are strongly decorrelated by agricultural activity or existence of vegetation over this region [43]. The short 90-day temporal threshold was set in order to mitigate this effect, and also resolve seasonal changes in time series.

A. Circuit Test

To further illustrate the accuracy of the geometric alignment, as well as the accuracy of the calculation of the interferometric baselines, we performed a circuit test for track 173 by summing up interferograms along the dashed lines shown in Fig. 4. The circuit had two segments. The time-increasing segment was the sum of 21 interferograms from October 29, 2014 to July 26, 2016, as shown with dashed blue lines in Fig. 4. The time-decreasing segment spanned the same time interval, and is shown by the dashed red lines in Fig. 4. Theoretically, the sum around this circuit should be zero except for possible phase noise due to decorrelation. The results are shown in Fig. 5, where the phase and coherence of the direct two-year interferogram are compared with the sum of 21 interferograms over the same time span. While the phase from a direct interferogram and the summed interferograms share similar features, the coherences are very different. The average coherence of the 21 interferograms is significantly higher than the coherence of the direct two-year interferogram. This provides improved phase recovery of the summed interferogram with respect to the direct interferogram. The closure test [Figs. 5(f) and S6 in the Supplementary Material] produces a very small phase residual (median of 0.013 mm, median absolute deviation of 0.97 mm), considering that we are summing up 42 interferograms spanning four years. This indicates the error introduced from data processing is small for deformation signals greater than ~1 mm/4yrs.

B. Atmospheric Correction and SBAS

The main objective of this analysis is to compute displacement time series for each of the ascending and descending stacks of SAR images to an accuracy of a few mm/yr, in order to better constrain the interseismic deformation of the region. Because atmospheric and ionospheric phase delays, as well as orbital and clock errors, are sometimes much greater than the ground deformation signal, we use the high redundancy of the interferograms to estimate and remove these errors. This is done in combination with SBAS time series estimation using an iterative approach described in [39]. They note that the phase of each interferogram $\Delta\phi$ can be decomposed into the following terms:

$$\Delta\phi_{ij} = \Delta\tau_{ij} + \alpha_j - \alpha_j + \varepsilon_{ij} \tag{1}$$

where $\Delta\tau$ is the deformation signal (steady in time), α is the phase error (turbulent in time) in each SAR image, and ε represents other errors, such as an inaccurate DEM or antenna noise. These α-related errors can be estimated and removed by means of common-point stacking, assuming they are randomly distributed in time. One important advantage of this stacking method is that it will capture the miss-registration errors at the same time, as they are also random in time. Together with this error correction, we applied a coherence-based SBAS method to compute time series for the CPGF region [10], [21], [36]. Instead of omitting low coherence pixels, this algorithm solves for the time series at every pixel while taking in coherence as weights [25] for the least squares problem. The short revisit times of the Sentinel-1A satellite, combined with the coherence-based SBAS, help mitigate strong decorrelation in this area.

C. Velocity and Displacement Time Series

The mean line-of-sight (LOS) velocity acquired for each track is shown in Fig. 6. Since there is no good quality GPS model for the region [26] to provide large spatial scale control on the InSAR data, we selected a point far from faults on the North America plate and set its displacement to zero for every interferogram; this provides a reference point for all other pixels. Note that this does not violate the closure test that is the preset rule for error estimation by common-point stacking. The displacement time series and atmospheric corrections for each epoch are provided in the Supplementary Material (Figs. S3 and S4). The maximum observed LOS velocity of the subsiding region is −178 mm/yr for track 173 and −157 mm/yr for track 166. The boundaries of the subsidence are well defined in LOS velocity map and the overall subsidence rate increases toward the east from the Cerro Prieto fault to the Imperial fault. More interestingly, the eastern margin of the subsidence terminates at the southern end of the Imperial fault, which may indicate that the fault acts as a barrier to subsurface fluid flow.

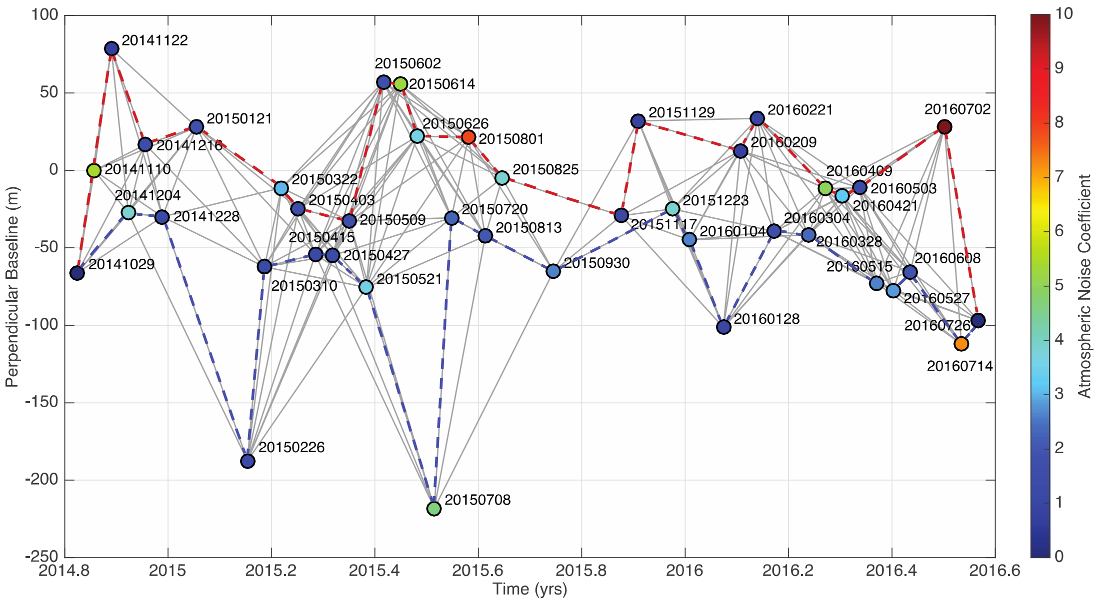

Fig. 4. Perpendicular baseline versus time plot for track 173 over CPGF. The dots represent acquisition dates and the gray lines denote interferometric pairs selected with a 200-m baseline threshold and 90-day temporal threshold. The colors of the dots indicate the atmospheric noise coefficient [39], with a larger value representing a stronger atmospheric noise contribution on that date. The red and blue dashed lines correspond to the interferograms used in the circuit test.

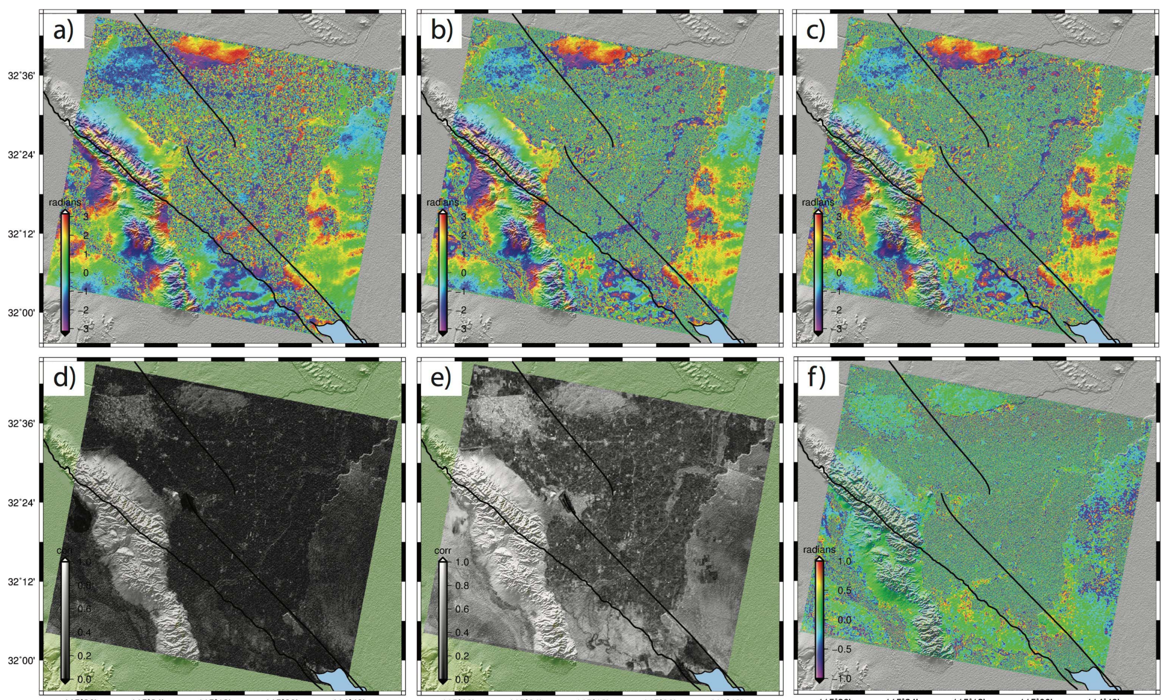

Fig. 5. Circuit test for the CPGF area on track 173. (a) Interferogram connecting October 29, 2014 and July 26, 2016 with (d) being its coherence. (b) Interferogram generated by adding up 21 interferograms following the dashed red line in Fig. 4, with (e) being their average coherence. (c) Interferogram generated by adding up 21 interferograms following the dashed blue line in Fig. 4. (f) Phase residual when adding up 42 interferograms along the dashed line circuit (median of 0.013 mm, median absolute deviation of 0.97 mm). The black lines are the nearby faults provided by the Centro de Investigación Científica y de Educación Superior de Ensenada (CICESE).

We decomposed the two LOS velocity maps into fault-parallel horizontal velocity and vertical velocity, by assuming the average fault azimuth to be N36.5° W [17]. The estimated maximum vertical subsidence is 163 mm/yr and the horizontal motion from east to west (over the mapped area) is roughly 40 mm/yr, in agreement with the overall change in velocity across these fault systems [2]. The large vertical deformation in the region of the CPGF is caused by removal of geothermal fluids [8]. If the CPGF were modeled by deflating Mogi source(s) one would expect significant horizontal motions in a direction pointing to the region of maximum subsidence (see [31]). Therefore our fault-parallel decomposition is not valid in this region and the original LOS data should be used for inverting for the Mogi sources [38]. In addition to the subsidence of the CPGF, we also observe significant subsidence at Heber geothermal field [black circle in Fig. 6(a)], although the maximum LOS velocity here is smaller, only around −60 mm/yr.

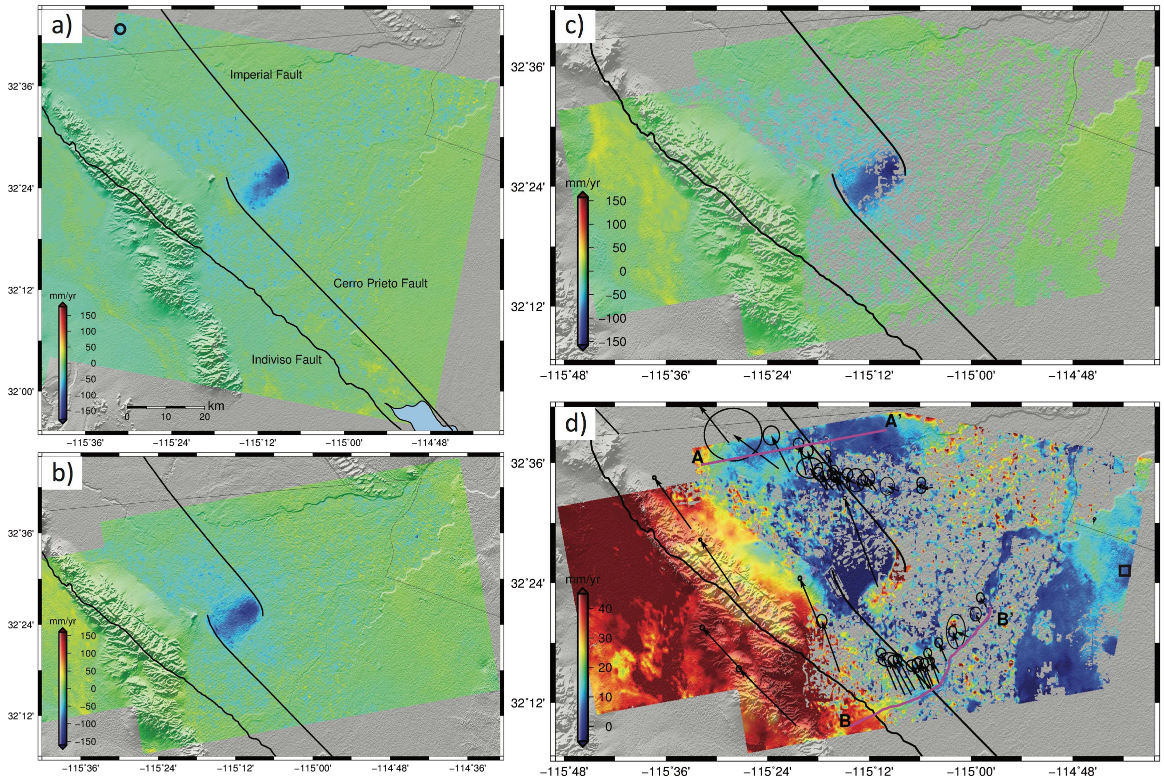

Fig. 6. Velocity map derived from analyzing 42 scenes, 201 interferograms (Fig. 4) from descending track 173, and 34 scenes 183 interferograms (Fig. S2 in the Supplementary Material) from ascending track 166. (a) LOS velocity map for track 173. (b) LOS velocity map for track 166. (c) and (d) Decomposed vertical velocity and fault-parallel velocity following [17], assuming the average fault azimuth to be N36.5° W. A 0.15 coherence threshold was used to mask the data projected. The black lines are the faults and black arrows are GPS survey mode data in North America fixed reference frame with circles denoting the uncertainty. The black circle in (a) is the location of the Heber geothermal field and the black square in (d) is the location we pinned down to zero in the SBAS processing.

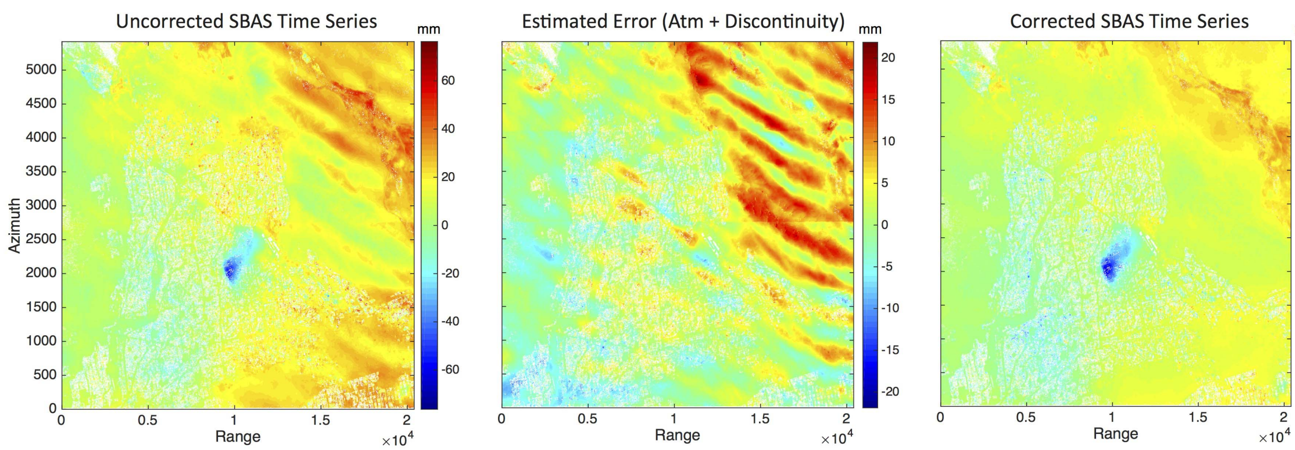

Fig. 7. Error reduction by common-point stacking. (Left) Uncorrected displacement in radar coordinates on April 27, 2015 with respect to the first acquisition on October 29, 2014, estimated with coherence-based SBAS for descending track 173. (Center) Error estimated by the common-point stacking method [39]. (Right) Displacement acquired with coherence-based SBAS after removing the estimated error from every interferograms.

As mentioned in Section II, there is usually a small phase offset (<1.4 mm) between bursts. We do not correct for this offset because it has the same temporal characteristics as the atmospheric delay, in that it is common in interferograms that share an acquisition date and random in time. Therefore, we use the common-point stacking approach [39] to magnify, estimate, and remove the burst offsets together with the atmospheric noise. Fig. 7 shows the estimated error on April 24, 2015 from the time series calculated for descending track 173. The uncorrected deformation map [Fig. 7 (Left)] is contaminated by an atmospheric delay having the characteristic pattern as a lee-wave [41]. Also, there are small burst discontinuities around azimuth line 2700 and 4100. These features are absorbed into the estimated error [Fig. 7 (Center)]. After applying the correction, the deformation time series are considerably flatter [Fig. 7 (Right)]. A full comparison for track 173 can be found in Movie S1 in the Supplementary Material, where the uncorrected time series is more turbulent in time and the corrected is much cleaner. It also brought our attention that, during this study, the assumption that the atmosphere is equally strong across the full scene is occasionally biased by topographical barriers.

When different sources of atmospheric signal come in to the same scene, the stronger one will potentially dominate the atmospheric correction sequence, thus a prioritized area (usually your area of interest) needs to be selected ahead to avoid such situation. Fig. 8 shows the corrected and uncorrected LOS displacement time series at the CPGF. The corrected time series are very clean, while the uncorrected time series are quite noisy, even though they were computed with the same smoothness parameter using coherence-based SBAS [36].

D. Comparison With GPS Data

Over the past six years, we have deployed two linear GPS arrays across the Imperial and Cerro Prieto faults to better characterize their velocity gradient. The monuments consist of stainless steel couplers cemented into massive concrete structures. The GPS antennas are screwed directly into the couplers for accurate and rapid deployment. To obtain the GPS position estimates we used GAMIT/GLOBK software [15] in ITRF2008 reference frame [1]. Site velocities were computed by least squares linear fitting to time variation of coordinates for each station and then rotated with respect to stable North America reference frame [3]. Velocity uncertainties are estimated within one-sigma confidence level [16]. We extracted fault-parallel velocity along two traces to compare with InSAR data. The extracted InSAR velocity is the mean value over 10×10-pixel ($\sim$180 m $\times$ 260 m) boxes along A–A′ and B–B′ traces as shown in Fig. 6(d), taking the standard deviation as the measurement uncertainty. The InSAR velocity is shifted to match the GPS, because during InSAR data processing, the point pinned to zero is not essentially zero if measured with GPS under North America fixed reference frame. The A–A′ trace is not extracted exactly along the GPS locations because these areas are not well correlated. However, the comparison shows good agreement across the Imperial Fault with an overall $\sim$30 mm/yr deformation across the fault [Fig. 9(a)]. The fast increase toward the western end suggests there is a hidden fault, as pointed out by [18], or possibly this sharp curve is biased by the subsidence signal from the nearby Heber geothermal field. The comparison also shows good agreement across the western side of the Cerro Prieto fault but poorer agreement on the eastern side. The InSAR measurements in this eastern area were extracted slightly south of the GPS line in the Colorado River valley where the correlation is the best. The InSAR to GPS differences in this region may be due to seasonal hydrologic signals, which would contaminate the frequent InSAR acquisitions, but would not be resolved by the less frequent GPS measurements. If we combine the GPS and InSAR data, the estimated deformation from east to west along B–B′ is close to 40 mm/yr, with a larger portion going across the Indiviso fault than the Cerro Prieto fault. The higher deformation rate over Indiviso fault may reflect continued postseismic deformation following the 2010 El-Mayor Cucapah earthquake [12].

IV. Discussion and Conclusion

We demonstrate a pure geometric algorithm for InSAR processing of TOPS data from the Sentinel-1A satellite. The accurate orbits and software result in phase differences at burst boundaries of generally less than 1.4 mm. Since this

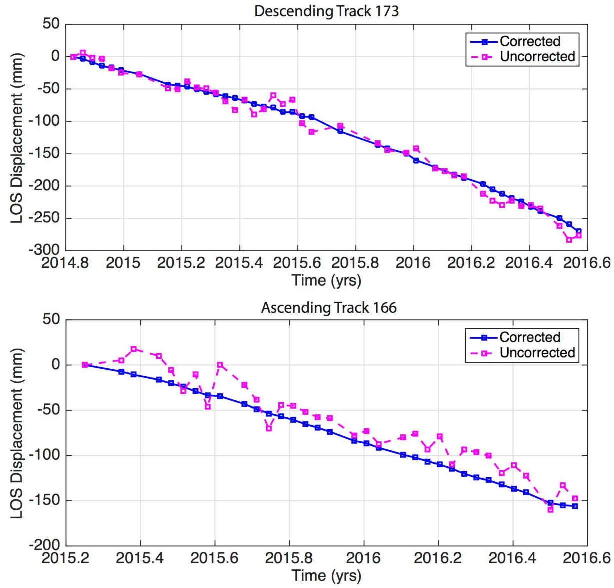

Fig. 8. LOS displacement time series at CPFG. (Top) Subsidence revealed by descending track 173 and (Bottom) ascending track 166. The magenta dashed lines are the time series without the error correction from [39], and the blue lines are the corrected time series. Both results used coherence-based SBAS [36] with the same smoothing parameter.

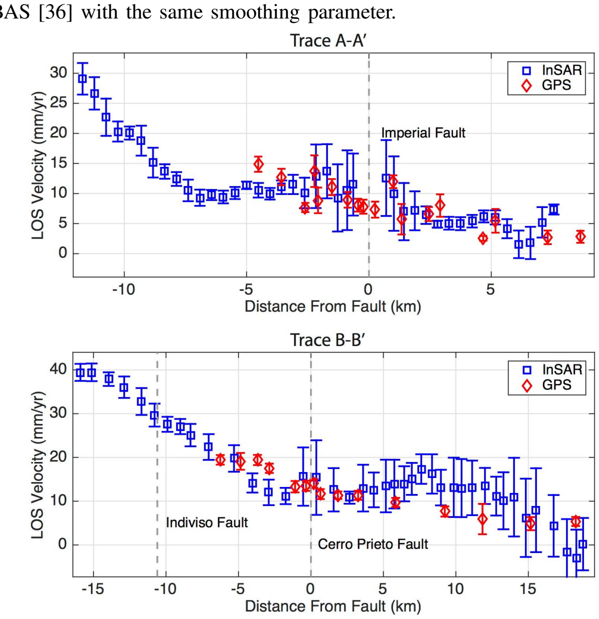

Fig. 9. Comparison between InSAR fault-parallel velocity map and GPS. InSAR velocity is extracted along the two magenta trace in Fig. 6(d). GPS data are projected to the fault-parallel direction.

error is far smaller than the atmospheric phase delays and could be associated with azimuthal misalignment, ionospheric variations, or true ground motion, we propose that the ESD method for tuning the azimuth alignment is not needed. Moreover, there are three significant advantages to pure geometric alignment with no ESD. First by aligning all repeat images to a single master, circuit closure is guaranteed. This closure is required for common-point stacking and long-timespan SBAS time series. Second, long time series can be processed incrementally, so that when a new SAR image is added it can be geometrically aligned to the master image and interferograms can be constructed from any of the other images. Third, interseismic motion can produce a significant along-track shift that can be corrected using an accurate plate tectonic model rather than estimated with ESD. For example, consider a long-timespan interferogram of a stable plate interior that is moving at 40 mm/yr in the satellite azimuth direction with respect to the International Terrestrial Reference Frame. The satellite orbit is computed in this fixed reference frame so after a decade of plate motion the azimuth shift of 0.4 m will cause a large burst mismatch of 8 mm. The coherence between the reference and repeat images may not be sufficient for accurate ESD, but since the tectonic motion is well known, an accurate azimuth shift can be applied during the processing. The main disadvantage to not performing ESD is that the small residual mismatch can lower the coherence at the burst boundaries [33].

We demonstrate the combined accuracy of the Sentinel-1 radar and orbits as well as the GMTSAR software by performing a circuit sum of 42 interferograms. The circuit closes to less than 1 mm, which is much smaller than the atmospheric error. This accurate closure ensures that long-timespan interferograms can be accurately constructed from SBAS analyses of redundant short-timespan interferograms. This approach provides a means to extract interseismic motion in agricultural areas where one- and two-year interferograms are largely decorrelated.

We applied the method of pure geometric alignment, common-point stacking for error estimation, and coherence-based SBAS to ascending (42) and descending (34) acquisitions in the region surrounding the CPGF. The error estimation technique works well due to the small baselines, short-timespan, and regular cadence of Sentinel-1A satellite. The improved coverage facilitates the combination ascending and descending LOS mean velocity grids into vertical and fault-parallel grids. The fault-parallel estimates show adequate agreement with two dense GPS profiles across the Imperial and Cerro Prieto faults. This new analysis provides refined estimates of three important crustal deformation signals in the region.

1) We produce the first complete map of the area of high subsidence rate at the step-over between the Imperial and Cerro Prieto faults. The estimated subsidence rate is higher now (~160 mm/yr) than in the past (120–140 mm/yr). Considering that the CPGF is currently only 11 m above sea level, the region will be at sea level in just 65 years if the current rate continues.
2) We show that the Imperial fault does not accommodate the full 40 mm/yr of strike slip motion across the region and there is significant deformation across unmapped faults in the western Mexicali valley and further to the west.
3) We observe that currently the Cerro Prieto fault accommodates less than half of the full plate motion. Our analysis shows significant motion across the Indiviso fault and faults further to the west. This could be continued near-field postseismic deformation following the 2010 El-Mayor Cucapah earthquake. These three crustal deformation signals will be more fully resolved in the next few years as the Sentinel-1B begins its systematic coverage of the region to complement the critical measurements from Sentinel-1A.

ACKNOWLEDGMENT

The authors would like to thank the three anonymous reviewers for their valuable suggestions, the European space agency for the extraordinary data open policy on the Sentinel-1 mission, and the ASF and UNAVCO for archiving the data and the precise orbital products. The fault traces were provided by CICESE.

REFERENCES

[1] Z. Altamimi, X. Collilieux, and L. Métivier, "ITRF2008: An improved solution of the international terrestrial reference frame," *J. Geodesy*, vol. 85, no. 8, pp. 457–473, 2011, doi: 10.1007/s00190-011-0444-4.

[2] R. A. Bennett, W. Rodi, and R. E. Reilinger, "Global Positioning System constraints on fault slip rates in southern California and northern Baja, Mexico," *J. Geophys. Res., Solid Earth*, vol. 101, no. B10, pp. 21943–21960, 1996.

[3] G. Blewitt *et al.* (2005). Stable North American reference frame (SNARF): First release, working group rep. UNAVCO, Boulder, CO, Canada. [Online]. Available: https://www.unavco.org/projects/past284projects/snarf/snarf.html

[4] F. De Zan, "Accuracy of incoherent speckle tracking for circular Gaussian signals," *IEEE Geosci. Remote Sens. Lett.*, vol. 11, no. 1, pp. 264–267, Jan. 2014.

[5] F. De Zan, P. Prats-Iraola, R. Scheiber, and A. Rucci, "Interferometry with TOPS: Coregistration and azimuth shifts," in *Proc. 10th Eur. Conf. Synth. Aperture Radar*, Jun. 2014, pp. 1–4.

[6] H. Fattahi, P. Agram, and M. Simons, "A network-based enhanced spectral diversity approach for TOPS time-series analysis," *IEEE Trans. Geosci. Remote Sens.*, vol. 55, no. 2, pp. 777–786, Feb. 2017.

[7] J. Fernández, D. Escobar, H. Peter, and P. Féménias, "Copernicus POD service operations—Orbital accuracy of Sentinel-1A and Sentinel-2A," in *Proc. Int. Symp. Space Flight Dyn.*, Munich, Germany, Oct. 2015.

[8] E. Glowacka, O. Sarychikhina, F. Suárez, F. A. Nava, and R. Mellors, "Anthropogenic subsidence in the Mexicali Valley, Baja California, Mexico, and slip on the Saltillo fault," *Environ. Earth Sci.*, vol. 59, no. 7, pp. 1515–1524, 2010.

[9] G. Gomba, F. R. González, and Z. De Zan, "Ionospheric phase screen compensation for the Sentinel-1 TOPS and ALOS-2 ScanSAR modes," *IEEE Trans. Geosci. Remote Sens.*, vol. 55, no. 1, pp. 223–235, Jan. 2017.

[10] P. J. González and J. Fernández, "Error estimation in multitemporal InSAR deformation time series, with application to Lanzarote, Canary Islands," *J. Geophys. Res., Solid Earth*, vol. 116, no. B10, 2011, Art. no. B10404.

[11] P. J. González *et al.*, "The 2014–2015 eruption of Fogo volcano: Geodetic modeling of Sentinel-1 TOPS interferometry," *Geophys. Res. Lett.*, vol. 42, no. 21, pp. 9239–9246, 2015.

[12] A. Gonzalez-Ortega *et al.*, "El Mayor-Cucapah (M_w 7.2) earthquake: Early near-field postseismic deformation from InSAR and GPS observations," *J. Geophys. Res. Solid Earth*, vol. 119, no. 2, pp. 1482–1497, 2014, doi: 10.1002/2013JB010193.

[13] R. F. Hanssen, *Radar Interferometry: Data Interpretation and Error Analysis*, vol. 2. New York, NY, USA: Springer, 2001.

[14] T. Herring, R. W. King, and S. M. McClusky, "Introduction to GAMIT/GLOBK release 10.4," Dept. Earth, Atmos. Planetary Sci., Massachusetts Inst. Technol., Cambridge, MA, USA, 2010.

[15] T. Herring, "MATLAB tools for viewing GPS velocities and time series," *GPS Solutions*, vol. 7, no. 3, pp. 194–199, 2003.

[16] E. O. Lindsey, Y. Fialko, Y. Bock, D. T. Sandwell, and R. Bilham, "Localized and distributed creep along the southern San Andreas Fault," *J. Geophys. Res., Solid Earth*, vol. 119, no. 10, pp. 7909–7922, 2014.

[17] E. O. Lindsey and Y. Fialko, "Geodetic constraints on frictional properties and earthquake hazard in the Imperial Valley, southern California," *J. Geophys. Res., Solid Earth*, vol. 121, no. 2, pp. 1097–1113, Feb. 2016.

[18] A. Meta, J. Mittermayer, P. Prats, R. Scheiber, and U. Steinbrecher, "TOPS imaging with TerraSAR-X: Mode design and performance analysis," *IEEE Trans. Geosci. Remote Sens.*, vol. 48, no. 2, pp. 759–769, Feb. 2010.

[19] N. Miranda, "Definition of the TOPS SLC deramping function for products generated by the S-1 IPF," Eur. Space Agency, Paris, France, Tech. Rep. COPE-GSEG-EOPG-TN-14-0025, 2015, p. 15.

[20] L. Marotti, P. Prats, R. Scheiber, S. Wollstadt, and A. Reigber, "Differential SAR interferometry with TerraSAR-X TOPS data: Mexico city subsidence results," in *Proc. 9th Eur. Conf. Synth. Aperture Radar (EUSAR)*, Apr. 2012, pp. 677–680.

[21] D. Massonnet and J.-C. Souyris, *Imaging With Synthetic Aperture Radar*. Boca Raton, FL, USA: CRC Press, 2008.

[22] P. Prats-Iraola, R. Scheiber, L. Marotti, S. Wollstadt, and A. Reigber, "TOPS interferometry with TerraSAR-X," *IEEE Trans. Geosci. Remote Sens.*, vol. 50, no. 8, pp. 3179–3188, Aug. 2012.

[23] W. H. Press, S. A. Teukolsky, W. T. Vetterling, and B. P. Flannery, "Golden section search in one dimension," in *Numerical Recipies in C: The Art of Scientific Computing*, vol. 2. New York, NY, USA: Cambridge Univ. Press, 1992, pp. 390–395.

[24] P. A. Rosen *et al.*, "Synthetic aperture radar interferometry," *Proc. IEEE*, vol. 88, no. 3, pp. 333–382, Mar. 2000.

[25] D. T. Sandwell *et al.*, "The SCEC community geodetic model V1: Horizontal velocity grid," presented at the SCEC Annu. Meeting, 2016.

[26] D. Sandwell, R. Mellors, X. Tong, M. Wei, and P. Wessel, "Open radar interferometry software for mapping surface deformation," *EOS, Trans. Amer. Geophys. Union*, vol. 92, no. 28, p. 234, 2011, doi: 10.1029/2011EO280002.

[27] E. Sansosti, P. Berardino, M. Manunta, F. Serafino, and G. Fornaro, "Geometrical SAR image registration," *IEEE Trans. Geosci. Remote Sens.*, vol. 44, no. 10, pp. 2861–2870, Oct. 2006.

[28] O. Sarychikhina, E. Glowacka, R. Mellors, and F. S. Vidal, "Land subsidence in the Cerro Prieto Geothermal Field, Baja California, Mexico, from 1994 to 2005: An integrated analysis of DInSAR, leveling and geological data," *J. Volcanol. Geothermal Res.*, vol. 204, nos. 1–4, pp. 76–90, 2011.

[29] O. Sarychikhina, E. Glowacka, B. Robles, F. A. Nava, and M. Guzmán, "Estimation of seismic and aseismic deformation in Mexicali Valley, Baja California, Mexico, in the 2006–2009 period, using precise leveling, DInSAR, geotechnical instruments data, and modeling," *Pure Appl. Geophys.*, vol. 172, no. 11, pp. 3139–3162, 2015.

[30] P. Segall, *Earthquake and Volcano Deformation*. Princeton, NJ, USA: Princeton Univ. Press, 2010.

[31] R. Scheiber, M. Jäger, P. Prats-Iraola, F. De Zan, and D. Geudtner, "Speckle tracking and interferometric processing of TerraSAR-X TOPS data for mapping nonstationary scenarios," *IEEE J. Sel. Topics Appl. Earth Observ. Remote Sens.*, vol. 8, no. 4, pp. 1709–1720, Apr. 2015.

[32] M. Shirzaei, R. Bürgmann, and E. J. Fielding, "Applicability of Sentinel-1 Terrain Observation by Progressive Scans multitemporal interferometry for monitoring slow ground motions in the San Francisco Bay Area," *Geophys. Res. Lett.*, vol. 44, no. 6, pp. 2733–2742, Mar. 2017.

[33] M. Simons and P. A. Rosen, "Interferometric synthetic aperture radar," in *Treatise on Geophysics*, vol. 3, G. Schubert, Ed. Amsterdam, The Netherlands: Elsevier, 2007, pp. 391–446, doi: 10.1016/B978-044452748-6.00059-6.

[34] W. H. F. Smith and P. Wessel, "Gridding with continuous curvature splines in tension," *Geophysics*, vol. 55, no. 3, pp. 293–305, 1990.

[35] X. Tong and D. Schmidt, "Active movement of the cascade landslide complex in Washington from a coherence-based InSAR time series method," *Remote Sens. Environ.*, vol. 186, pp. 405–415, Dec. 2016.

[36] R. Torres *et al.*, "GMES Sentinel-1 mission," *Remote Sens. Environ.*, vol. 120, pp. 9–24, May 2012.

[37] D. T. Trugman, A. A. Borsa, and D. T. Sandwell, "Did stresses from the Cerro Prieto Geothermal Field influence the El Mayor-Cucapah rupture sequence?" *Geophys. Res. Lett.*, vol. 41, no. 24, pp. 8767–8774, 2014.

[38] E. Tymofyeyeva and Y. Fialko, "Mitigation of atmospheric phase delays in InSAR data, with application to the eastern California shear zone," *J. Geophys. Res., Solid Earth*, vol. 120, no. 8, pp. 5952–5963, 2015.

[39] D. W. Vasco, C. Wicks, Jr., K. Karasaki, and O. Marques, "Geodetic imaging: Reservoir monitoring using satellite interferometry," *Geophys. J. Int.*, vol. 149, no. 3, pp. 555–571, 2002.

[40] P. W. Vachon, O. M. Johannessen, and J. A. Johannessen, "An ERS 1 synthetic aperture radar image of atmospheric lee waves," *J. Geophys. Res.*, vol. 99, no. C11, pp. 22483–22490, 1994, doi: 10.1029/94JC01392.

[41] M. Wei and D. T. Sandwell, "Decorrelation of L-band and C-band interferometry over vegetated areas in California," *IEEE Trans. Geosci. Remote Sens.*, vol. 48, no. 7, pp. 2942–2952, Jul. 2010.

[42] N. Yague-Martinez, P. Prats-Iraola, and F. De Zan, "Coregistration of interferometric stacks of Sentinel-1A TOPS data," in *Proc. 11th Eur. Conf. Synth. Aperture Radar (EUSAR)*, Jun. 2016, pp. 1–6.

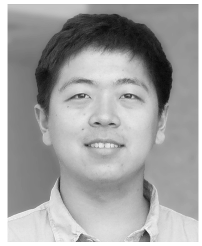

Xiaohua Xu received the B.S. degree in geophysics from the University of Science and Technology of China, Hefei, China, in 2012. He is currently pursuing the Ph.D. degree in geophysics with the Scripps Institution Oceanography, University of California, San Diego, CA, USA, with the specilizationon interferometric synthetic aperture radar (InSAR) technique and its application to geophysical problems.

His research interests include how to correctly determine tectonic deformation using appropriate InSAR techniques and evaluate the strain accumulation during different tectonic processes.

David T. Sandwell received the B.S. degree in physics from the University of Connecticut, Mansfield, CT, USA, in 1975, and the Ph.D. degree in geophysics and space physics from the University of California, Los Angeles, CA, USA, in 1981.

Since 1994, he has been a Professor of geophysics with the Scripps Institution of Oceanography, University of California, San Diego, CA, USA. His research interests include satellite geodesy crustal deformation and marine geophysics.

Dr. Sandwell is a member of the US National Academy of Sciences and a Fellow of the American Geophysical Union.

Ekaterina Tymofyeyeva was born in Odessa, Ukraine. She received the B.S. degree in physics from The College of New Jersey, Ewing Township, NJ, USA, in 2009, and the M.S. degree in earth science from the University of California, San Diego, CA, USA, in 2013, where she is currently pursuing the Ph.D. degree with the Scripps Institution of Oceanography.

Her research interests include the applications of interferometric synthetic aperture radar and global positioning system measurements to the study of crustal deformation.

Alejandro González-Ortega received the B.S. degree in physics from the University of Baja California, Tijuana, Mexico, in 2003, and the Ph.D. degree in earth sciences from the Centro de Investigacion Cientifica y Educacion Superior de Ensenada (CICESE), Ensenada, Mexico, in 2014.

From 2014 to 2016, he was a Post-Doctoral Research with the Scripps Institution of Oceanography, University of California, San Diego, CA, USA, and was affiliated with Solid Earth Group, Jet Propulsion Laboratory. Since 2017, he has been an Assistant Researcher with the Seismology Department, CICESE. His research interests include the use of the global navigation satellite system and interferometric synthetic aperture radar data for measuring crustal deformation.

Xiaopeng Tong was born in Beijing, China. He received the B.S. degree from Peking University, Beijing, in 2007, and the Ph.D. degree in earth science from the University of California, San Diego, CA, USA, in 2013.

He was a Research Assistant with the University of California from 2007 to 2013, and a Postdoctoral Researcher with the University of Washington, Seattle, WA, USA, from 2014 to 2017. His research interests include interferometric synthetic aperture radar and its application to earth science.